Available online at www.sciencedirect.com
ScienceDirect
C. R. Mecanique 334 (2006) 545–554
COMPTES RENDUS MECANIQUE
http://france.elsevier.com/direct/CRAS2B/

Observation, analysis and modelling in complex fluid media

Modelling and simulation of powder-snow avalanches

Jocelyn Étienne [a,1], Marie Rastello [b], Emil J. Hopfinger [c,*]

[a] *LMC IMAG, BP 53, 38041 Grenoble cedex 9, France*
[b] *LMFA-ECL, 36, avenue Guy de Collongue, 69134 Ecully cedex, France*
[c] *LEGI/CNRS, B.P. 53, 38041 Grenoble cedex 9, France*

Available online 6 September 2006

Abstract

Finite volume release gravity currents of large density contrast on steep slopes, representing powder-snow avalanches, are simulated numerically using a dynamic mesh adaptation technique. This technique allows to treat large Reynolds numbers and large density contrast flows, but it is (presently) restricted to two dimensions. Comparison of numerical results with experiments in the Boussinesq limit shows that 2D simulations capture the essential flow dynamics. The physics of powder-snow avalanches is analysed on hand of the similarity model developed by Rastello and Hopfinger (2004) and briefly reproduced here. The numerical simulations provide the closure parameters required in this model and give access to the flow structure. The non-Boussinesq effect is to decrease substantially the spatial growth in height and to increase the aspect ratio, hence the overall flow structure. ***To cite this article: J. Étienne et al., C. R. Mecanique 334 (2006).***

Résumé

Modélisation et simulation d'avalanches de neige poudreuse. Des courants gravitaires formés par le déversement d'un volume fini de fluide de densité élevée sur des pentes abruptes, représentant des avalanches de neige poudreuse, sont simulées numériquement en utilisant une technique de maillage adaptatif dynamique. Cette technique permet de traiter des nombres de Reynolds élevés et des écoulements à fortes différences de densité mais elle est (actuellement) limitée au cas bidimensionnel. Une comparaison entre résultats numériques et expérimentaux dans la limite de Boussinesq montre que les simulations 2D capturent l'essentiel de la dynamique. La physique des avalanches de neige poudreuse est analysée à l'aide du modèle de similarité développé par Rastello and Hopfinger (2004) et brièvement reproduit ici. Les simulations numériques fournissent les paramètres de fermeture nécessaires à ce modèle et donnent accès à la structure de l'écoulement. L'effet non-Boussinesq est de diminuer substantiellement l'accroissement spatial de la hauteur et d'accroître le rapport d'aspect, donc toute la structure de l'écoulement. ***Pour citer cet article : J. Étienne et al., C. R. Mecanique 334 (2006).***

Keywords: Computational fluid mechanics; Avalanches; Gravity effects; Modelling; Numerical simulations

Mots-clés : Mécanique des fluides numérique ; Avalanches ; Effets dus à la gravité ; Modélisation ; Simulations numériques

* Corresponding author.
E-mail addresses: j.etienne@damtp.cam.ac.uk (J. Étienne), marie.rastello@ec-lyon.fr (M. Rastello), emil.hopfinger@hmg.inpg.fr (E.J. Hopfinger).
[1] Present address: DAMTP, University of Cambridge, Wilberforce Road, Cambridge CB3 0WA, UK.

1631-0721/$ – see front matter
doi:10.1016/j.crme.2006.07.010

1. Introduction

Powder-snow avalanches are dense clouds moving down steep slopes. The extra weight of the cloud is due to the suspended snow particles in air of volume concentration 0.4 to 4%. This results in a bulk density of about 2 to 30 times the air density. During the motion, air is entrained which leads to a dilution and growth of the cloud and, depending on the flow conditions, snow can also be picked-up from the underlying snow cover which may cause a continuous acceleration of the avalanche. In order to reach velocities of the order of 100 m/s, a value often quoted for powder-snow avalanches [1,2], a continuous down-slope acceleration is required. This large front velocity and, consequently, the large turbulent velocity, assures that the snow particles of diameter $d_p \approx 0.5$ to 1 mm and density $\rho_p \approx 400$ to 900 kg/m^3 remain suspended and that an avalanche is capable of picking up further snow from the snow cover as long as the volume concentration is less than the saturation concentration. Furthermore, the Stokes number $St = \tau_p/\tau_f$, expressing the characteristic particle time scale τ_p to flow time scale $\tau_f \approx H/U_f$, where U_f is the avalanche front velocity and H its height, is less than 0.1, noting that because of the relatively large particle Reynolds numbers, τ_p is evaluated for a particle drag larger than the Stokes drag. For the case of a particle stratified shear layer Meiburg et al. [3] showed that when the Stokes number is about 0.1 the particle loading has an effect similar to that of a single phase stratified fluid. Therefore, it can be assumed that the suspension cloud behaves like a single phase gravity flow of large density difference.

Beghin et al. [4] conducted laboratory experiments with finite volume release gravity currents, forming dense clouds on slopes, using small density ratio (Boussinesq) saline solutions. Rastello and Hopfinger [5] (from here on referred to as RH) made similar experiments with saline solutions and in addition with finite volume release turbidity currents moving over a sediment layer on slopes. The turbidity clouds showed a similar behaviour to the single phase saline clouds. A similarity model has been developed by RH which contains as closure parameters an air (ambient fluid) entrainment coefficient E_c and a sediment entrainment coefficient E_s. An additional parameter is the aspect ratio of cloud length to height k. These coefficients were obtained from the experiments in the Boussinesq limit and used in the model to predict avalanche velocity variation, noting that the avalanche velocity depends on E_c and E_s but not on k.

Further insight can be gained from direct numerical simulations especially in the case of large density ratios. It has been shown by Étienne et al. [6] that large Reynolds number simulations of large density ratio gravity flows are possible by using a dynamic grid adaptation technique. The drawback is that these techniques are presently limited to two-dimensions. Although the turbulence structure is three-dimensional, it can be assumed that the dynamics of the cloud movement is a two-dimensional process, controlled by the large scale structures of principal vorticity component normal to flow direction. Two-dimensional simulations of gravity currents [7] and of lock-exchange flows [8,6] for instance are in good agreement with experiments although the turbulence structure is three-dimensional.

In Section 2 the similarity model is presented and compared with measurements of the front velocity reported for the Sion Valley avalanche by Dufour et al. [9]. In Section 3 the 2D numerical simulations are first applied to Boussinesq clouds for conditions corresponding to the experiments of RH. Then, numerical results are presented for the same conditions but with the density ratio increased to 20. These results show clearly the non-Boussinesq effect on the flow structure; the acceleration length is substantially larger and the growth rate is reduced.

2. Similarity model

To a good approximation a powder-snow avalanche can be considered as a single phase dense cloud moving down steep slopes. Arguments supporting this assumption are developed above in Section 1. During the motion the size increases and, for a given slope angle, the shape remains similar, that is the aspect ratio of height to length remains constant.[2] Fig. 1 shows a schematic representation of the cloud shape with the definition of the relevant variables.

The momentum, mass and volume per unit width conservation equations are respectively:

$$\frac{\mathrm{d}(\rho_a k_v + \rho)AU}{\mathrm{d}t} = \Delta\rho A g \sin\theta - C_f \rho_b U^2 L \tag{1}$$

[2] This is a first approximation because, as the present numerical simulations indicate, the aspect ratio depends on density ratio which decreases with distance.

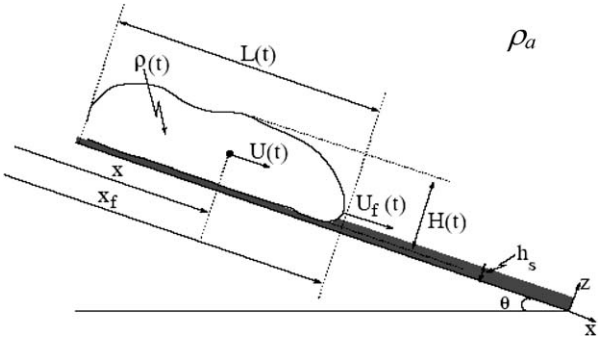

Fig. 1. Definition sketch.

Fig. 1. Schéma de définition.

$$\frac{\mathrm{d}\Delta\rho A}{\mathrm{d}t} = \beta\Delta\rho_s h_s U = E_s \Delta\rho_s L U \tag{2}$$

$$\frac{\mathrm{d}A}{\mathrm{d}t} = E_c U\sqrt{A} = E_c \frac{\sqrt{S_1}}{S_2} U P \tag{3}$$

where $\rho = \rho_p C + \rho_a(1-C)$, $\Delta\rho = \rho - \rho_a$, $A = S_1 k H^2$, $P = S_2\sqrt{HL}$, $k(\theta) = L/H$, C_f is the bottom friction coefficient, h_s the snow cover depth, β is the fraction of the snow cover entrained along the avalanche path, S_1 and S_2 are shape factors, k_v is the added mass coefficient and E_c and E_s are air (ambient fluid) and snow (sediment) entrainment coefficients respectively. The subscript a stands for air or ambient fluid, p for particles, s for snow cover (sediment) and b for bed. After transforming time into space by setting $U = \mathrm{d}x/\mathrm{d}t$, Eq. (1) can be integrated (see [5]) in the form:

$$U = \frac{\sqrt{2KMx + (KB+GM)x^2 + \frac{2}{3}(KN+GB)x^3 + \frac{1}{2}GNx^4}}{M + Bx + Nx^2} \tag{4}$$

where

$$K = (\Delta\rho_0 A_0) g \sin\theta$$
$$M = (k_v + 1)\rho_a A_0 + \Delta\rho_0 A_0$$
$$N = (1+k_v)\frac{\rho_a}{4} E_c^2$$
$$B = \beta\Delta\rho_s h_{s+}(1+k_v)\rho_a E_c A_0^{1/2}$$
$$G = \beta\Delta\rho_s h_s g \sin\theta$$

In the integration of Eq. (1) it was assumed that at $x = 0$, $U = 0$ but $A = A_0$ and $L_0/H_0 = k$.

Eq. (3) gives (keeping S_1 constant):

$$H = H_0 + \frac{E_c}{2\sqrt{kS_1}} x \tag{5}$$

and from Eq. (2) the buoyancy variation with distance is obtained in the form:

$$\Delta\rho A = \Delta\rho_0 A_0 + \beta\Delta\rho_s h_s x \tag{6}$$

Typical values for a powder-snow avalanche, the Sion Valley avalanche for instance [9] are: $A_0 = 200\ \mathrm{m}^2$, $\Delta\rho_0 = 150\ \mathrm{kg/m}^3$, average slope angle $\theta = 25°$, $\Delta\rho_s = 150\ \mathrm{kg/m}^3$, $h_s = 1$ m. The shape factors are closely approximated by an elliptic shape, namely $S_1 \cong 0.8$ and $S_2 \cong 2.4$, while k_v is taken constant, equal to 0.5. It has been shown by RH that the velocity predicted by this similarity model is in good agreement with measured avalanche velocities when taking for the closure parameters E_c and β, respectively the values $E_c \approx 0.25$ (for $\theta = 25°$) and $\beta = 1$, i.e., the whole snow cover is incorporated along the avalanche path. Bottom friction is practically unimportant on steep slopes. This is demonstrated by integrating equation (1) numerically with and without bottom friction. It is, however, the principal

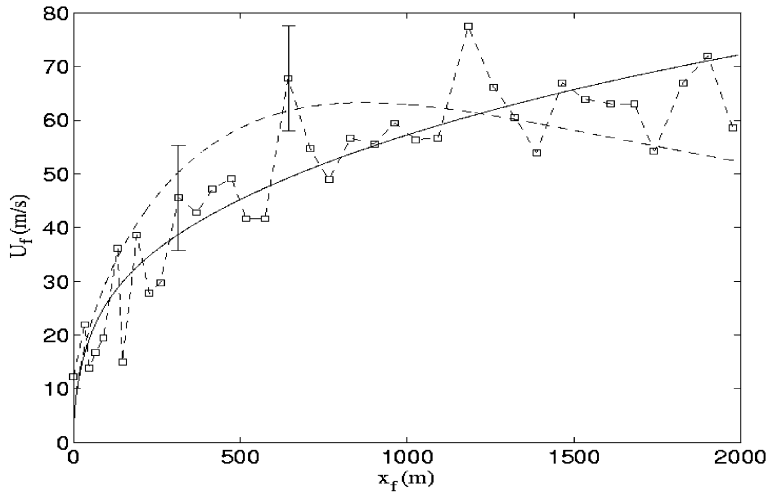

Fig. 2. Avalanche front velocity $U_f = U(1 + E_c k^{1/2}/4S_1^{1/2})$ as a function of front position. -□-, measured avalanche front velocity [9]; —, model prediction for $\theta = 25°$, $E_c = 0.25$, $\beta = 1$ and $C_f = 0$; - - -, model prediction for $\beta = 0$ (no snow entrainment).

Fig. 2. Vitesse du front d'avalanche $U_f = U(1 + E_c k^{1/2}/4S_1^{1/2})$ en fonction de la position du front. -□-, vitesse du front d'avalanche mesurée [9] ; —, prédiction du modèle pour $\theta = 25°$, $E_c = 0.25$, $\beta = 1$ et $C_f = 0$; - - -, prédiction du modèle pour $\beta = 0$ (sans entrainement de neige).

retarding force when the avalanche moves onto nearly horizontal ground. Fig. 2 shows a comparison of the model predictions (neglecting bottom friction) with measurements. In this figure the front velocity U_f rather than the mass centre velocity is plotted because this velocity is directly accessible to measurements. The two are related by the spatial growth in cloud length. For the prediction of this spatial growth of an avalanche, it is necessary to know, in addition to the air entrainment coefficient E_c, the aspect ratio k. Observations suggest that $k \approx 6$ for the Sion Valley avalanche.

Field observations of powder-snow avalanches are difficult and rare and measurements of the variation of the front velocity with distance became available only recently [9]. Measurements of velocity and density distributions inside an avalanche are, however, nearly impossible, although some attempts were made using radar. Turbulence closure models (turbulent energy-dissipation models in particular), are used for practical applications and give useful information for quasi-steady flows [10] but give no information about the time dependency of local quantities (density and velocity variations). For this reason, and in order to understand the avalanche dynamics in more detail, we turn to laboratory experiments and numerical simulations. Laboratory experiments are, unfortunately, limited to Boussinesq flows [11,4,5]. Only lock-exchange flow experiments have been performed for density ratios of about 20 using gases [12]. It is hardly feasible to use gases for gravity current or dense cloud experiments on slopes because of the large gas volumes needed. Direct numerical simulations or large eddy simulations are, therefore, necessary tools of research in this area.

By using the automatic mesh adaptation technique, developed for gravitational flows by Étienne et al. [6], it is possible to reach large Reynolds numbers (order 10^5) and large density differences in direct numerical simulation. Since direct numerical simulations of dense clouds on steep slopes seem not to have been conducted previously it is necessary to validate numerical results by experiments at least in the Boussinesq limit. For this reason the conditions of the numerical simulations presented in the following Section 3.3 are the same as in the experiments of RH. The simulations are then extended to a density ratio of 20 to quantify the non-Boussinesq effect.

3. Numerical simulations

3.1. Governing equations

We consider the isothermal flow of a single phase fluid with large density variations, and equal, constant dynamic viscosity η under the conditions described above. For a perfect mixture of two incompressible fluids, of density ρ_d (the heavier one) and of density ρ_a (the lighter one), the local density is $\rho = \rho_d \Phi + \rho_a(1 - \Phi)$, where Φ is the local

volume fraction of the fluid of density ρ_d. The density contrast is defined as $\alpha = (\rho_d - \rho_a)/\rho_a$, and the density can be rewritten as $\rho = \rho_a(1+\alpha\Phi)$. Lengths are non-dimensionalized according to the scale $L_r = \sqrt{A_0}$ of initial release, $\tilde{x} = x/L_r$ and velocities by the terminal velocity $U_r = \sqrt{\alpha g L_r}$ of a fluid element of density ρ_d in the ambient fluid of density ρ_a, $\tilde{\mathbf{u}} = \mathbf{u}/U_r$. Times are non-dimensionalized as $\tilde{t} = tU_r/L_r$. Momentum and mass conservation of the cloud and ambient air are given by the Navier–Stokes equations,

$$(1+\alpha\Phi)\frac{\mathrm{D}\tilde{\mathbf{u}}}{\mathrm{D}\tilde{t}} = -\nabla p + \frac{1}{Re}\operatorname{div}\left(2\,\mathrm{D}\tilde{\mathbf{u}} - \frac{2}{3}\operatorname{div}\tilde{\mathbf{u}}I\right) - \frac{1+\alpha\Phi}{\alpha}\mathbf{k} \tag{7}$$

$$\alpha\frac{\mathrm{D}\Phi}{\mathrm{D}\tilde{t}} + (1+\alpha\Phi)\operatorname{div}\tilde{\mathbf{u}} = 0 \tag{8}$$

where the Reynolds number is defined as $Re = \rho_a U_r L_r/\eta$, and $\mathrm{D}\tilde{\mathbf{u}} = (\nabla\tilde{\mathbf{u}} + \nabla\tilde{\mathbf{u}}^{\mathrm{T}})/2$. Since the fluids are miscible, we cannot assume $\mathrm{D}\rho/\mathrm{D}t = 0$, but rather that there are mass diffusion fluxes in the flow governed by Fick's law. This yields [6]:

$$\frac{\mathrm{D}\Phi}{\mathrm{D}\tilde{t}} + \Phi\operatorname{div}\tilde{\mathbf{u}} = \frac{1}{Re\,Sc}\nabla^2\Phi \tag{9}$$

where the Schmidt number is defined as $Sc = \eta/\rho_a\mathcal{D}$, with $\mathcal{D}$ a reference diffusivity. Initial conditions consist of given distribution of ρ initially, the velocity being set to zero everywhere. No inflow or outflow across the boundaries of the flow domain has been considered, thus boundary conditions are always $\nabla\Phi\cdot\mathbf{n} = 0$, with either no-slip boundary conditions ($\tilde{\mathbf{u}}|_{\partial\Omega} = 0$) or zero wall friction ($\tilde{\mathbf{u}}\cdot\mathbf{n} = 0$ and $\sigma\cdot\mathbf{n} - [(\sigma\cdot\mathbf{n})\cdot\mathbf{n}]\mathbf{n} = \mathbf{0}$, where $\mathbf{n}$ is the wall normal and $\sigma = 2\mathrm{D}\tilde{\mathbf{u}} - (2/3)\operatorname{div}\tilde{\mathbf{u}}I$).

System (7)–(9) was proposed by Étienne et al. [6] for the simulation of gas mixtures of high density contrast. An algorithm was devised for its resolution in the framework of finite elements and used for simulations of lock-exchange flows in two dimensions. These flows are a good test for high density contrast flow simulation, because there have been experimental and theoretical studies, and measurements for density contrasts up to $\alpha \approx 20$ are available [12]. Numerical results are shown to be in good agreement with these measurements.

3.2. Numerical technique

Due to high Reynolds numbers and the flow structure, the flow of the buoyant clouds considered in this article present features of very different spatial scales (time-dependent strong local velocity and density gradients), which make dynamic mesh adaptation a necessity, although this technique is still poorly developed in 3D [13]. The very high computational cost of three-dimensional DNS limits other approaches to Reynolds number lower than 10^3 [7]. The numerical simulations presented here are thus restricted to the two dimensions x and z, and make use of the dynamic mesh adaptation features of the mesh generator BAMG [14].

The remaining difficulty is to simulate efficiently both the transport and viscous terms on a general mesh. This is done by the Lagrange–Galerkin method [15], which consists in using the method of characteristics to discretise directly the material derivative along with finite elements for the discretisation in space. Étienne and Saramito [16] have designed an algorithm for Eqs. (7)–(9) and shown optimal error estimates, and have implemented it in the open source free software RHEOLEF [17]. The finite element spaces are continuous, piecewise quadratic for the velocity and volume fraction, and continuous, piecewise linear for the pressure. The mesh refinement is an iterative process at each time step: a first estimate of the solution is calculated on a coarse mesh, and then the mesh is repeatedly refined and the solution recalculated until some mesh invariance is achieved. This is usually done in four re-meshing iterations, with the final mesh having refinement ratios of order 10^3 between the coarsest triangle size and the finest one, with an approximate total of 5×10^5 degrees of freedom.

3.3. Results for Boussinesq clouds

The simulations are first performed for a Boussinesq cloud which allows comparison with experiments. A volume of fluid of density ρ_d and length $l_0 = 20$ cm and $h_0 = 6.5$ cm, $A_0 = h_0 l_0 = 130$ cm^2 and reference length $L_r = \sqrt{A_0} = 11.4$ cm, is suddenly released in a stagnant fluid of density ρ_a, $\alpha = (\rho_d - \rho_a)/\rho_a = 0.02$, and of depth $6L_r$ and length $20L_r$. The slope angle is $\theta = 32°$.

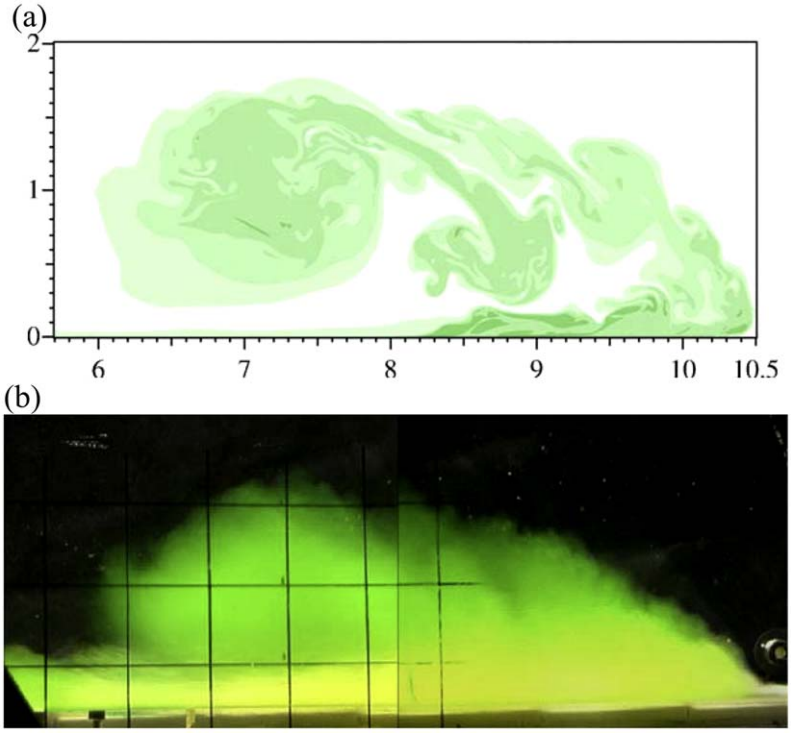

Fig. 3. Aspect of the cloud, (a) numerical simulation with $\alpha = 0.02$ and $Re = 10^5$, (b) experiments [5]. In the experiments the grid spacing is 5 cm and in (a) the coordinates are non-dimensionalized by $L_r = 11.4$ cm.

Fig. 3. Aspect du nuage, (a) simulation numérique avec $\alpha = 0{,}02$ et $Re = 10^5$, (b) expériences [5]. Dans l'expérience la taille des mailles est 5 cm et dans (a) les coordonnées sont normalisées par $L_r = 11{,}4$ cm.

Fig. 3 shows a qualitative comparison of the density contours. What is of interest here is the similar shape indicating a length to height ratio k of about 3. It should be noted, however, that there are large fluctuations in k (about $\pm 10\%$) due to the time variations of the large eddy structure.

In Fig. 4 the simulated front velocity is compared with the experimental values of RH. There is a good agreement when $Re = U_r L_r \rho_a / \eta = 10^5$, where $U_r = \sqrt{\alpha g L_r}$. In the simulation free slip conditions on the bottom were used (this corresponds to $C_f = 0$ in the model). The calculated and experimentally determined spatial growth rates are compared in Fig. 5. There is a reasonably good agreement in a range around the velocity maximum ($2 < x_f/L_r < 9$). At large distances the 2D simulations give a larger growth rate. This is to be expected since in 2D the large eddies are more persistent than in 3D. Note that x_f is measured from the gate of release of the dense fluid. The virtual origin was taken as $x_0 = -3L_r$ in all the plots presented here.

3.4. Results for non-Boussinesq clouds

The non-Boussinesq flow simulations were conducted for $\alpha = 19$ and a Reynolds number $Re = 10^5$. The flow domain was increased to $50L_r$, while the depth is reduced to $4L_r$. The initial volume released and the slope angle were kept the same as in the Boussinesq case allowing a direct comparison. Fig. 6 shows an image of the density contrast of the flow; the change in flow structure is clearly seen by comparing this image with Fig. 3.

In Fig. 7 the calculated mass centre velocity is plotted as a function of the position of the mass centre, non-dimensionalized by L_r. The calculated velocity for $\alpha = 0.02$ as well as the solution of Eqs. (1)–(3), taking $\beta = 0$, $C_f = 0$ and $E_c = 0.26$ are presented for comparison. There is good agreement with the model but the calculated velocity decreases more rapidly than is predicted by the model. This may be due to a larger entrainment of ambient fluid in the 2D simulations.

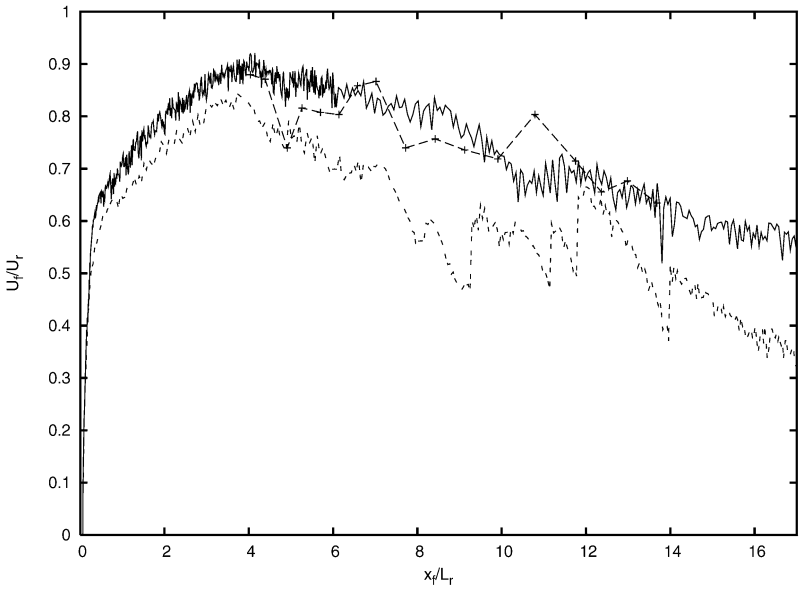

Fig. 4. Front velocity vs. front position, —, numerical simulation with $\alpha = 0.02$ and $Re = 10^5$, - -, numerical simulation with $\alpha = 0.02$ and $Re = 10^4$, $- + -$, experimental results of RH, with $Re_{\exp} = \rho_a L_r \sqrt{\alpha g L_r}/\mu_a \approx 3 \times 10^4$.

Fig. 4. Vitesse du front en fonction de la position du front, —, simulation numérique avec $\alpha = 0.02$ et $Re = 10^5$, - -, simulation numérique avec $\alpha = 0{,}02$ et $Re = 10^4$, $- + -$, résultats de RH, avec $Re_{\exp} = \rho_a L_r \sqrt{\alpha g L_r}/\mu_a \approx 3 \times 10^4$.

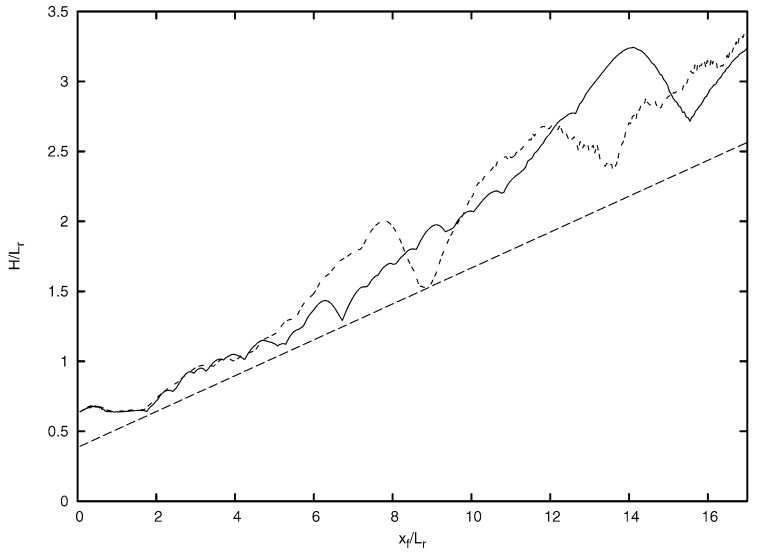

Fig. 5. Height of the cloud vs. front position, —, numerical simulation with $\alpha = 0.02$, $\theta = 32°$ and $Re = 10^5$, - - - -, numerical simulation with $\alpha = 0.02$ and $Re = 10^4$, – –, experimental results of RH approximated by $\frac{dH}{dx_f} = 3.6 \times 10^{-3}\theta + 0.013$ (H is determined with respect to the virtual origin at $x_f = -3L_r$).

Fig. 5. Hauteur du nuage en fonction de la position du front, —, simulation numérique avec $\alpha = 0{,}02$, $\theta = 32°$ et $Re = 10^5$, - - - -, simulation numérique avec $\alpha = 0{,}02$ et $Re = 10^4$, – –, résultats expérimentaux de RH approchés par $\frac{dH}{dx_f} = 3.6 \times 10^{-3}\theta + 0.013$ (H est déterminé par rapport à l'origine virtuelle en $x_f = -3L_r$).

In Fig. 8 the non-dimensional height is plotted versus front position for $\alpha = 0.02$ and $\alpha = 19$. There is clearly a substantial decrease in the spatial growth rate of the cloud when the density ratio is large. The dashed straight line represents the experimentally determined growth rate approximated by $H = (3.6 \times 10^{-3}\theta + 0.013)(x_f - x_0)$,

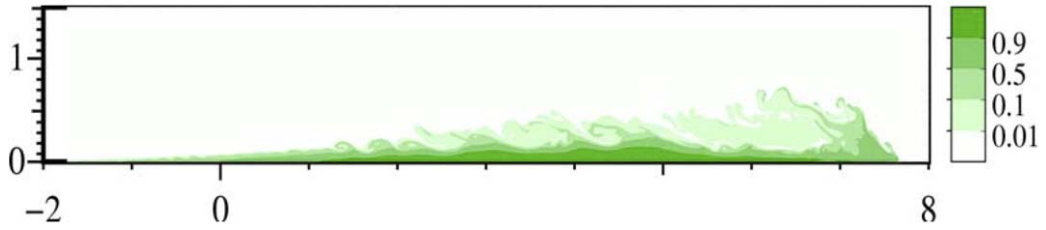

Fig. 6. Aspect of the cloud in a numerical simulation with $\alpha = 19$ and $Re = 10^5$: excess density Φ in colour code as a function of the space variables x and z; coordinates are non-dimensionalized by L_r.

Fig. 6. Aspect du nuage simulé numériquement avec $\alpha = 19$ et $Re = 10^5$: excès de densité Φ en couleur en fonction des variables spatiales x et z ; les coordonnées sont normalisées par L_r.

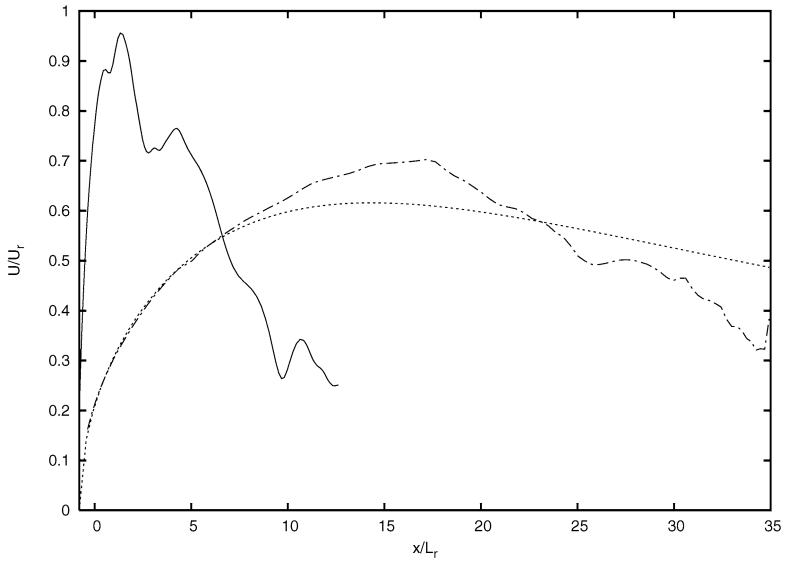

Fig. 7. Mass centre velocity of the cloud versus non-dimensional mass centre position, ---, numerical simulation for $\alpha = 19$, $\theta = 32°$ and $Re = 10^5$; —, numerical simulation for $\alpha = 0.02$ and $Re = 10^5$; ⋯, integrated model equation (1) for no snow-entrainment, $\beta = 0$ and $E_c = 0.26$, $k_v = 0.5$, $C_f = 0$. The velocity is non-dimensionalized by $U_r = \sqrt{\alpha g L_r}$.

Fig. 7. Vitesse du centre de masse du nuage en fonction de la position sans dimension du centre de masse, ---, simulation numérique pour $\alpha = 19$, $\theta = 32°$ et $Re = 10^5$; —, simulation numérique pour $\alpha = 0{,}02$ et $Re = 10^5$; ⋯, equation modèle intégrée (1) sans entraînement de neige, $\beta = 0$ et $E_c = 0{,}26$, $k_v = 0{,}5$, $C_f = 0$. La vitesse est normalisée par $U_r = \sqrt{\alpha g L_r}$.

and the dotted line corresponds to the extrapolation to a non-Boussinesq cloud proposed by RH given by $\frac{\mathrm{d}H}{\mathrm{d}x}\big|_{\mathrm{NB}} = \frac{\mathrm{d}H}{\mathrm{d}x}\big|_{\mathrm{B}} \frac{1+\sqrt{\rho_a/\rho_b}}{2}$, where subscripts NB and B stand for non-Boussinesq and Boussinesq. The model predicts reasonably well the decrease in growth rate when the density ratio is large (note that for the bed density ρ_b the value of the initial density was used, $\rho_b/\rho_a = 20$). RH assumed that the spatial growth in cloud length does not depend on density ratio. The numerical simulations confirm this assumption (Fig. 9). The aspect ratio of the avalanche (cloud), $k = L/H$ is, therefore, larger for large density difference clouds and is approximated by $k_{\mathrm{NB}} = k_{\mathrm{B}} \frac{2}{1+\sqrt{\rho_a/\rho_b}}$. Consequently the entrainment coefficient E_c is reduced by $E_{\mathrm{cNB}} = E_{\mathrm{cB}} \sqrt{(1 + \sqrt{\rho_a/\rho_b})/2}$. For a Boussinesq cloud on a slope of 32° the value of E_c is approximately 0.32, which gives for the non-Boussinesq cloud with $\alpha = 19$ a value of $E_c \approx 0.25$. This justifies the value used for calculating the front velocity in Fig. 7.

It may be noted that the numerical simulations indicate a decrease in the spatial growth in height and an increase in the growth in length when $x_f/L_r > 12$. The reason for this is that the stratification causes the large eddies to collapse when the eddy Froude number falls below about 1. In the similarity model, where it is assumed that the density of the cloud is inversely proportional to the cloud volume, the overall Froude number is always larger than 1. In the simulated flow (and probably in reality) this is not the case.

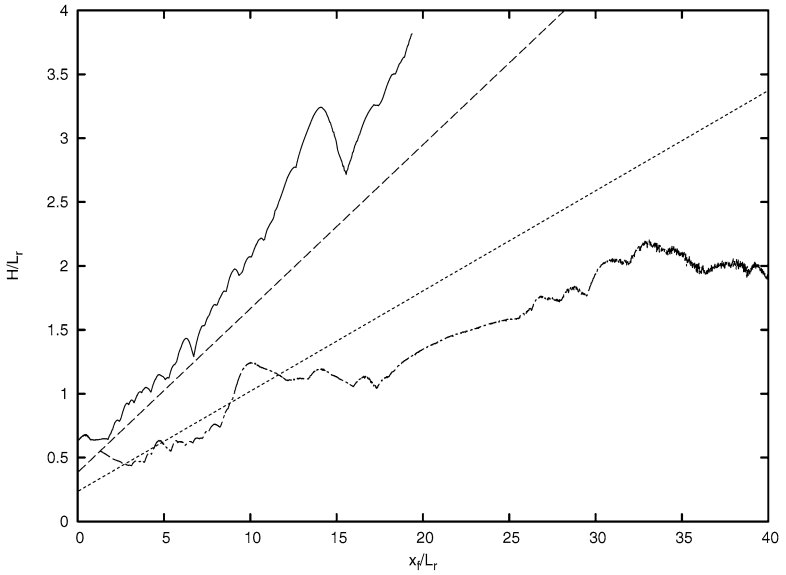

Fig. 8. Non-dimensional height of the cloud versus front position. —, numerical simulation with $\alpha = 0.02$ and $Re = 10^5$, ---, numerical simulation with $\alpha = 19$ and $Re = 10^5$, – –, experimental results of RH for Boussinesq clouds, ···, extrapolation of experimental results to non-Boussinesq conditions.

Fig. 8. Hauteur sans dimension du nuage en fonction de la position du front. —, simulation numérique avec $\alpha = 0{,}02$ et $Re = 10^5$, ---, simulation numérique avec $\alpha = 19$ et $Re = 10^5$, – –, résultats expérimentaux de RH pour des nuages de Boussinesq, ···, extrapolation des résultats expérimentaux aux conditions non-Boussinesq.

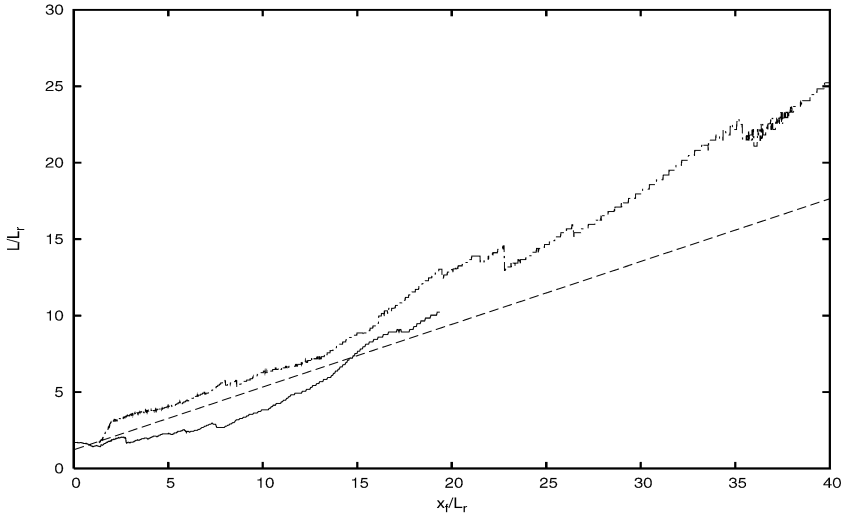

Fig. 9. Non-dimensional length of the cloud versus front position. —, numerical results for $\alpha = 0.02$; ---, $\alpha = 19$. The dashed straight line corresponds to $L = kH$ with $k_{\mathrm{NB}} = k_{\mathrm{B}} \frac{2}{1+\sqrt{\rho_a/\rho_b}}$.

Fig. 9. Longueur sans dimension du nuage en fonction de la position du front. —, résultats numérique pour $\alpha = 0{,}02$; ---, $\alpha = 19$. La ligne droite en trait discontinu correspond à $L = kH$ avec $k_{\mathrm{NB}} = k_{\mathrm{B}} \frac{2}{1+\sqrt{\rho_a/\rho_b}}$.

4. Conclusions

To our knowledge the simulations presented in this paper are the first numerical simulations of large density difference, finite volume release gravity currents on steep slopes forming dense clouds. The finite element scheme used

with dynamic mesh adaptation allows to reach sufficiently large Reynolds numbers but simulations are limited to two dimensions. A comparison of numerical results with experiments in the Boussinesq limit shows that the essential physics is well captured by 2D such simulations. The simulations apply to powder-snow avalanches under the assumption that avalanches can be treated as a single phase, large density difference flow. This assumption is justified by the value of the Stokes number ($St < 0.1$) and is further supported by the similarity model presented in Section 2 which compares well with measured avalanche velocities. The closure parameters in this similarity model were determined from laboratory experiments in the Boussinesq limit and extrapolated to non-Boussinesq clouds by RH. To a good approximation the present numerical simulations support these theoretical extrapolations.

References

[1] E.J. Hopfinger, Snow avalanche motion and related phenomena, Annu. Rev. Fluid Mech. 15 (1983) 47–76.
[2] K. Hutter, Avalanche dynamics, in: V.P. Singh (Ed.), Hydrology of Disasters, Kluwer Academic Publishers, Dordrecht, 1996.
[3] E. Meiburg, E. Wallner, A. Pagella, A. Riaz, C.J.J. Haertel, F. Necker, Vorticity dynamics of dilute two-way-coupled particle-laden mixing layers, J. Fluid Mech. 421 (2000) 185–227.
[4] P. Beghin, E.J. Hopfinger, R.E. Britter, Gravitational convection from instantaneous sources on inclined boundaries, J. Fluid Mech. 107 (1981) 407–422.
[5] M. Rastello, E.J. Hopfinger, Sediment-entraining suspension clouds: a model of powder-snow avalanches, J. Fluid Mech. 509 (2004) 181–206.
[6] J. Étienne, E.J. Hopfinger, P. Saramito, Numerical simulations of high density ratio lock-exchange flows, Phys. Fluids 17 (2005) 036601.
[7] C.J.J. Haertel, E. Meiburg, F. Necker, Analysis and direct numerical simulation of the flow at a gravity-current head. Part 1. Flow topology and front speed for slip and no-slip boundaries, J. Fluid Mech. 418 (2000) 189–212.
[8] V.K. Birman, J.E. Martin, E. Meiburg, The non-Boussinesq lock-exchange problem. Part 2: high resolution simulations, J. Fluid Mech. 537 (2005) 125–144.
[9] F. Dufour, U. Gruber, W. Ammann, Avalanches : études réalisées dans la Vallée de la Sionne en 1999, Les Alpes 2 (2001) 9–15.
[10] P. Sampl, T. Zwinger, Avalanche simulation with SAMOS, Ann. Glaciol. 38 (2004) 393–398.
[11] R.E. Britter, P.F. Linden, The motion of the front of a gravity current travelling down an incline, J. Fluid Mech. 99 (1980) 531–543.
[12] H.P. Groebelbauer, T.K. Fanneløp, R.E. Britter, The propagation of intrusion fronts of high density ratios, J. Fluid Mech. 250 (1993) 669–687.
[13] P.-L. George, Sur la construction de maillages, Congres Français de Mecanique, Troyes, 2005.
[14] F. Hecht, BAMG: Bidimenisonal Anisotropic Mesh Generator, http://www-rocq1.inria.fr/gamma/cdrom/www/bamg/eng1.htm, INRIA, Rocquencourt, France, 1997.
[15] M. Bercovier, O. Pironneau, Characteristics and the finite elements method, in: T. Kawai (Ed.), Finite Element Flow Analysis, Proceedings of the 4th Int. Symp. on Finite Elements Methods in Flow Problems, Tokyo, North-Holland, 1982, pp. 67–73.
[16] J. Étienne, P. Saramito, A priori error estimates of the Lagrange–Galerkin method for Kazhikhov–Smagulov type systems, C. R. Acad. Sci. Paris, Ser. I (2005), in press.
[17] P. Saramito, N. Roquet, J. Étienne, RHEOLEF, a finite element environment, http://www-lmc.imag.fr/lmc-edp/Pierre.Saramito/rheolef, LMC, Grenoble, France, 2003.